Nanoscale Advances

ROYAL SOCIETY OF CHEMISTRY

PAPER

View Article Online
View Journal | View Issue

Cite this: *Nanoscale Adv.*, 2022, **4**, 2913

First-principles design of hetero CoM (M = 3d, 4d, 5d block metals) double-atom catalysts for oxygen evolution reaction under alkaline conditions†

Eoyoon Lee,[a] Sun Hee Choi[c] and Hyung Chul Ham *[ab]

As an extension of single-atom catalysts, the development of double-atom catalysts with high electrocatalytic activity for the oxygen evolution reaction (OER) is vital to facilitate hydrogen production and industrial applications. The CoM (M = 3d, 4d, 5d block metals) homo and double-atom catalysts supported on nitrogen-doped graphene (CoM/N_4G) were prepared for electrochemical water oxidation under alkaline conditions, and the electrocatalytic activity was studied through density functional theory (DFT) calculations. The hetero CoCu/N_4G double-atom catalyst indicated the highest OER activity with an onset potential of 0.83 V, while the homo Co_2/N_4G catalyst showed a higher onset potential of 1.69 V. The decoupled strain, dopant, and configurational effects based on the notable differences between the homo Co_2/N_4G and CoCu/N_4G explained the enhanced OER activity, implying that the Cu dopant has a crucial impact on boosting the reactivity by reducing the affinity of reaction intermediates. The enhancement could also be understood from the perspective of the electron structure characteristic through d-orbital resolved density of states (ORDOS) (d_{z^2}, d_{xz}, d_{yz}, d_{xy}, and $d_{x^2-y^2}$) analysis. From the ORDOS analysis, we found an apparent alteration of the key orbitals between Co_2/N_4G (d_{z^2}, d_{xz}, and d_{yz}) and CoCu/N_4G (d_{z2}, d_{xz}, d_{yz}, and d_{xy}) with a substantial change in the overlap ratio (X_d). This theoretical study offers beneficial insights into developing a strategy for efficient OER catalysts utilizing a double-atom structure.

Received 15th February 2022
Accepted 30th May 2022

DOI: 10.1039/d2na00107a

rsc.li/nanoscale-advances

Introduction

Water electrolysis using renewable energy is one of the most promising hydrogen production methods, because carbon dioxide (one of the main molecule for global warming) is not generated during the production and as a high purity of hydrogen can be obtained.[1–4] However, in water electrolysis systems, the hydrogen evolution reaction (HER) at the cathode is limited by the oxygen evolution reaction (OER) at the anode because of the sluggish kinetics and large operation potential of the OER.[5–8] Thus, novel metal-based catalysts, such as Ir or Ru oxides, are generally used as OER catalysts;[9,10] however, their high cost and low atom-utilization efficiency make them difficult for industrial applications.[11,12] Thus, the development of a cost-effective catalyst with high activity is needed for efficient hydrogen production. For this reason, many researchers have made efforts to enhance the catalytic activity through the particle size and morphology control of the catalysts or using a variety of support materials and dopants.[13–20]

Recently, the single-atom catalysts (SACs) have been extensively investigated due to their maximized atomic utilization with unique properties and a large number of active sites when the isolated single atoms are stabilized through a strong interaction with the support materials.[21–28] Among those SACs, transition metal–nitrogen-doped carbon catalysts (M–N–C) are the most widely studied because of their good mechanical properties, excellent electrical conductivity, and high stability in acidic/alkaline conditions, showing superior catalytic activity for many electrochemical reactions, such as HER,[29,30] oxygen reduction reaction (ORR),[31,32] OER,[33] and N_2-reduction reaction (N_2RR).[34] Moreover, as an extension of SACs, double-atom catalysts (DACs) have also been vigorously studied for achieving better electrocatalytic performance than SACs with a modulated electronic structure of the active centers.[35–40] For example, Yang *et al.* reported that transition-metal-doped double-atom Fe catalysts on graphene substrates (Fe-TM_{DA}/GS) have more obvious advantages due to their lower Gibbs free energy variation for the potential determining step in the nitrogen-reduction reaction (NRR) compared to the single-atom Fe catalyst.[41] Aside from double-atom Fe catalysts, diverse DACs such as Pt_2/graphene, Ni–V/graphene, and Pd_2/graphene have

[a]*Department of Chemistry and Chemical Engineering, Education and Research Center for Smart Energy Materials and Process, Inha University, Incheon, 22212, South Korea. E-mail: ham.hyungchul@inha.ac.kr*

[b]*Program in Smart Digital Engineering, Inha University, Incheon, 22212, Republic of Korea*

[c]*Center for Hydrogen·Fuel Cell Research, Korea Institute of Science and Technology (KIST), Seoul, 02792, Republic of Korea*

† Electronic supplementary information (ESI) available. See https://doi.org/10.1039/d2na00107a

shown remarkable catalytic performance in the hydrolytic dehydrogenation of ammonia borane, CO oxidation, and formic acid dehydrogenation, respectively.[42–44] Nevertheless, the study of DACs for the OER has not been much reported to date.

Herein, we constructed CoM (M = 3d, 4d and 5d block metals) double atoms supported on nitrogen-doped graphene (CoM/N_4G), where the M metal atom was coordinated with the Co metal center, and then evaluated its structural stability. Then, the electrocatalytic activity of CoM/N_4G for the OER was estimated through density functional theory (DFT) calculations. The CoCu/N_4G catalyst with an onset potential of 0.83 V presented the best OER performance compared to the other CoM/N_4G. To better understand the mechanism of the activity enhancement, the strain, dopant, and configurational effects on CoCu/N_4G were decoupled and compared with those of the Co_2/N_4G catalyst so that we could clearly confirm the role of the Cu atom. In addition, we found the key descriptor representing the catalytic activity based on the 3d block-metal-introduced CoM/N_4G catalyst and explored additional CoM/N_4G catalysts employing 4d and 5d block metals. Finally, d-orbital resolved density of states (ORDOS) (d_{z^2}, d_{xz}, d_{yz}, d_{xy}, and $d_{x^2-y^2}$) analysis for the key intermediate adsorbed CoM/N_4G system was performed to reveal the significant properties for the electronic structure of the active metal center related to the catalytic activity.

Computational details

All of the calculations here were performed on the basis of spin-polarized density functional theory (DFT) using the Vienna *Ab initio* Simulation Package (VASP).[45] The generalized gradient approximation (GGA) of Perdew–Burke–Ernzerhof (PBE) was used to approximate the exchange–correlation interaction.[46–48] The projector-augmented wave (PAW) method was also employed to substitute the complicated interaction between the core ions and valence electrons.[49] The plane wave functions were expanded with an energy cutoff of 400 eV for a reasonable number of plane waves. For all of the calculated models, the geometry optimization and electronic structure calculations were carried out with the Monkhorst–Pack mesh of $4 \times 4 \times 1$ *k*-points to guarantee sufficient accuracy.[50] Ionic relaxation was conducted until the residual force was less than 5×10^{-2} eV $Å^{-1}$. In this study, the hetero CoM (M = 3d, 4d, and 5d block metals) double-atom catalysts were created by anchoring the CoM dimer into the di-vacancy site, which was associated with four N atoms (indicated by CoM/N_4G), and the *z*-direction was fixed with the vacuum size of 20 Å to avoid undesirable interaction between periodic boundaries. When determining the optimized structure of CoM/N_4G, nine types of geometry were considered. Then, the most stable geometry was determined by the formation energy calculation. The formation energy (ΔE_f) from Co/N_4G (a single Co atom) to CoM/N_4G is described as follows:

$$\Delta E_f = E_{CoM/N_4G} - E_{Co/N_4G} - E_M$$

where E_{CoM/N_4G}, E_{Co/N_4G}, and E_M are the total energies of the CoM/N_4G, Co/N_4G, and single-M systems, respectively. Here, the choice of M atom for the formation energy calculation was related to the preparation method of the double-atom catalyst in which the sputtering or atomic layer deposition was accepted for the utilization of a single atom.[51–53]

The adsorption energy (ΔE_{ads}) was used to measure the adsorption strength between the intermediates and CoM/N_4G surface, and the adsorption energy is defined by the following equation:

$$\Delta E_{ads} = E_{tot} - E_{sur} - E_{int}$$

where the E_{tot}, E_{sur}, and E_{int} mean the total energies of the adsorbed system, clean surface of the catalyst and the intermediate, respectively.

To predict the Gibbs free energy change (ΔG) depending on the individual reaction steps, we assumed an alkaline mechanism in which OH^- is oxidized to H_2O and O_2 with electron (e^-) release, and adopted the computational hydrogen electrode (CHE) approach.[54,55] According to the CHE approach, the Gibbs free energy of ($H^+ + e^-$) can be calculated by the free energy of $\frac{1}{2}H_2$ in the gas phase, assuming the equilibrium,

$$H^+ + e^- \leftrightarrow \tfrac{1}{2}H_{2(g)}$$

under standard conditions [pressure (p_{H_2}) = 1 bar, and temperature (T) = 298.15 K]. In addition, the corrected Gibbs free energies of $H_2O_{(l)}$ and $O_{2(g)}$ (where the O_2 molecule is hard to describe by DFT) were obtained from the following equations:

$$G_{H_2O_{(l)}} = G_{H_2O_{(g)}} + RT \ln \frac{p}{p_0}$$

$$G_{O_{2(g)}} = 2G_{H_2O_{(l)}} - 2G_{H_{2(g)}} + 4.92$$

where R is the gas constant, T corresponds to 298.15 K, and p and p_0 are 0.035 bar and 1 bar, respectively (we assumed that $H_2O_{(l)}$ at 298.15 K and 1 bar is considered to be in equilibrium with $H_2O_{(g)}$ at 298.15 K and 0.035 bar). As reported in the CHE method, the only difference between acidic conditions and alkaline conditions for the Gibbs free energy calculation is related to the reference electrodes, *i.e.*, the standard hydrogen electrode and reversible hydrogen electrode (SHE and RHE).[55] Moreover, those two electrodes can be linked as per the following equation by adding the correction (described as G_{pH}):

$$G_{pH} = k_B T \times pH \times \ln 10$$

$$eU_{RHE} = eU_{SHE} + k_B T \times pH \times \ln 10$$

where eU_{RHE}, eU_{SHE}, k_B, and T are the electrode potential relative to RHE, SHE, Boltzmann constant, and temperature. To consider the alkaline environment of the solvent, the pH value is set to pH = 14. Thus, the equation for the Gibbs free energy change with the variation of the electrode potential (U_{SHE}) can be expressed for both an acidic mechanism and alkaline mechanism by the equation:

$$\Delta G = \Delta E - T\Delta S + \Delta ZPE - n(eU_{SHE} + G_{pH})$$

where ΔE indicates the adsorption energy of a reaction intermediate; ΔS, ΔZPE, and G_{pH} are the entropy, zero-point energy and free energy correction depending on pH condition, respectively; and n denotes the number of electrons transferred in the reaction. The overlap ratio (X_d) in this work means the quantitative degree of p–d orbital overlap between the d orbitals of CoM (M = Co, Cu) and the p orbital of the adsorbed O atom. That is, the fraction of p–d orbital overlap in the total p orbital can be calculated by the following equation:

$$X_d = \frac{\int|\rho_d - \rho_p|d\varepsilon}{\int \rho_p d\varepsilon}$$

where X_d, ρ_d, ρ_p, and ε are the overlap ratio, d density of state, p density of state, and energy *versus* the Fermi energy, respectively.

Result and discussion

Mechanism of the oxygen evolution reaction in a homo Co_2 double-atom catalyst

In this study, on a homo Co_2 double-atom [indicated by Co_2/N_4G], we consider the following four steps for the oxygen evolution reaction (OER) [$4OH^- \rightarrow O_{2(g)} + 2H_2O_{(l)} + 4e^-$] under alkaline conditions.[56,57]

$$* + OH^- \rightarrow OH^* + e^-$$

$$OH^* + OH^- \rightarrow O^* + H_2O_{(l)} + e^-$$

$$O^* + OH^- \rightarrow OOH^* + e^-$$

$$OOH^* + OH^- \rightarrow * + O_{2(g)} + H_2O_{(l)} + e^-$$

The first step for the OER is the adsorption of OH^- on Co_2/N_4G, forming OH* (* denoted as the adsorbed state) and the release of an electron. Second, the adsorbed OH* reacts with OH^-, activating the O–H bond dissociation and in turn liberating H_2O, leaving O* and an electron behind. The third step is the reaction of adsorbed O* with OH^-, leading to the formation of OOH* and an electron. The final step is the formation of O_2, H_2O, and electron *via* O–H scission by the reaction of adsorbed OOH* with OH^-. On the other hand, the dissociative mechanism of OER (where the adsorbed O* directly forms O_2 without OOH* formation) is not stated in this study. This is because the direct formation of O_2 from O*, which is a chemical reaction, is a large endothermic reaction due to the strong O* adsorption on Co_2/N_4G (see Fig. S1†). Aside from Co_2/N_4G, all the CoM/N_4G catalysts showed endothermic energy for the formation of O_2 from O*.

Fig. 1 shows the calculated free energy diagram for the OER and the molecular configurations of OER intermediates on a Co_2/N_4G catalyst. Here, we attempted to find the most stable structure of a homo Co_2 double-atom supported on defective graphene by comparing the formation energies (ΔE_f) of six possible configurations (denoted as C1, C3, C4, C6, C8, and C9) (see Table 1 and Fig. 2), which indicated that the homo Co_2 double-atom was stabilized in the form of the C4 geometry ($\Delta E_f = -1.63$ eV) (where one Co atom is connected to a rectangular-shaped nitrogen, while the other Co atom is linked to a hexagonal-shaped nitrogen and carbons, resulting in the formation of the inclined Co_2 structure).

For a homo Co_2/N_4G catalyst, our DFT calculations predicted that the $OOH^* + OH^- \rightarrow * + O_{2(g)} + H_2O_{(l)} + e^-$ reaction [defined as the potential limiting step (PLS)] determined the whole O_2 evolution activity since that was the most energetically demanding step (requiring the largest Gibbs free energy change for the OER) among the reaction pathways of the OER, which led to an onset potential (as indicated by U_{onset}) of 1.69 V (over potential of 1.29 V). This was higher by 0.91 V than a previously reported Co oxide catalyst.[19] Next, to further enhance the OER activity of a homo Co_2/N_4G catalyst, we replaced one Co atom in the Co_2 double-atom by 3d block metals (M = Sc, Ti, V, Cr, Mn, Fe, Ni, Cu, and Zn).

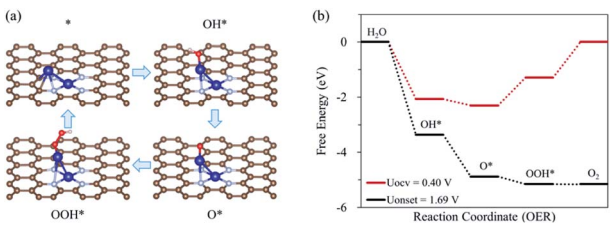

Fig. 1 (a) Schematic diagram of OER on Co_2/N_4G catalyst with the most favorable adsorption configuration of each intermediates, (b) free energy diagram depending on the OER pathway on Co_2/N_4G at OCV condition (U_{OCV} = 0.401 V) and onset potential.

Table 1 Formation energies (ΔE_f) (eV) of the considered CoM/N_4G configurations (C1)–(C9)

Catalyst	(C1)	(C2)	(C3)	(C4)	(C5)	(C6)	(C7)	(C8)	(C9)
$CoSc/N_4G$	−2.64	−2.82	−1.82	−3.22	−2.15	−3.11	−2.47	—	−2.62
$CoTi/N_4G$	−2.35	−3.42	−2.03	−3.09	—	−2.60	−3.02	−1.22	−2.10
CoV/N_4G	−1.73	−2.76	−0.71	−2.00	−1.54	−1.91	−2.09	−0.12	−0.98
$CoCr/N_4G$	−1.12	−0.53	1.18	—	−0.05	—	−0.08	2.04	—
$CoMn/N_4G$	−1.38	−0.04	1.13	—	−0.31	—	0.01	1.92	1.00
$CoFe/N_4G$	−1.66	−0.86	0.10	−1.64	−1.30	—	−1.25	0.96	0.37
Co_2/N_4G	−1.50	—	0.47	−1.63	—	−1.48	—	1.21	0.35
$CoNi/N_4G$	−1.59	−0.50	—	−1.63	−1.12	−1.63	−0.78	—	—
$CoCu/N_4G$	−1.40	2.22	—	—	1.43	—	1.81	—	—
$CoZn/N_4G$	−0.25	3.54	—	—	3.20	—	3.58	—	—

Structure of the hetero double-atom catalysts

As displayed in Fig. 2, the hetero double-atom catalysts (indicated by CoM/N_4G) could stably exist as one of nine possible configurations (denoted as C1–C9), whose stability could be quantitively understood by the calculation of the formation energy of the double atoms (ΔE_f). Table 1 compares the ΔE_f for the different configurations of the CoM/N_4G catalysts. We found that the most stable ensemble structures of the CoM/N_4G catalyst could be narrowed down to three geometries. That is, (1) the C1 geometry (we call the vertical Co double atom, where the Co atom of the CoM dimer was vertically bound to the rectangular-shaped four nitrogen atoms); CoCr ($\Delta E_f = -1.12$ eV), CoMn ($\Delta E_f = -1.38$ eV), CoFe ($\Delta E_f = -1.66$ eV), CoCu ($\Delta E_f = -1.40$ eV), and CoZn ($\Delta E_f = -0.25$ eV); (2) the C2 geometry (we called this the vertical M double atom, where the M atom of the CoM dimer was vertically associated with the rectangular-shaped four nitrogen atoms); CoTi ($\Delta E_f = -3.42$ eV), and CoV ($\Delta E_f = -2.76$ eV); (3) the C4 geometry (we called this the inclined hexagon M double atom, where the Co and M atoms were connected to the rectangular-shaped four nitrogen atoms and hexagonal-shaped carbon/nitrogen atoms, respectively); CoSc ($\Delta E_f = -3.22$ eV), and CoNi ($\Delta E_f = -1.63$ eV). The most stable ensemble geometries of the CoM/N_4G catalysts are shown in Fig. S2 in ESI Section.† Next, we examined the OER activity on the surface of the most stable CoM/N_4G catalysts.

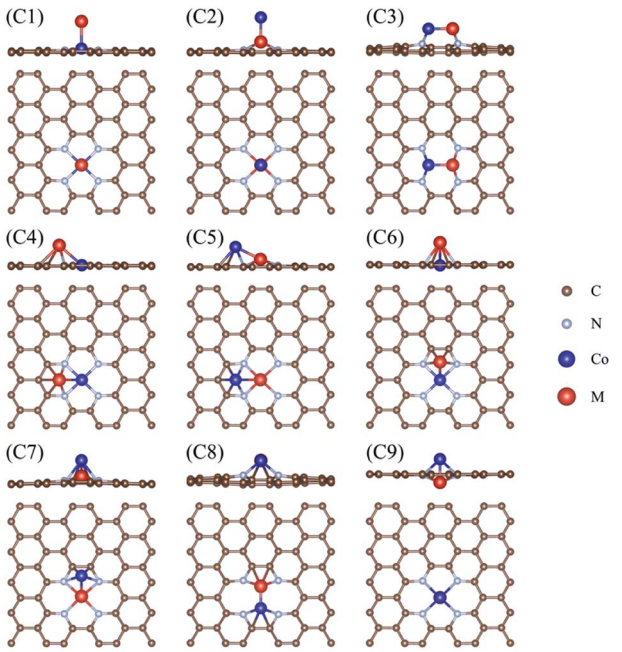

Fig. 2 Types of CoM/N_4G catalysts considered: (C1) and (C2) have a vertical bonding configuration, and (C3)–(C9) have horizontally or diagonally combined features with a different coordination of N or C atoms.

Electrocatalytic OER activity

Fig. 3 shows the Gibbs free energy diagram for OER on the hetero CoM/N_4G catalysts. We found that the hetero CoCu ($U_{onset} = 0.83$ V), CoMn ($U_{onset} = 1.57$ V), CoNi ($U_{onset} = 1.51$ V), and CoZn ($U_{onset} = 1.44$ V) double-atom catalysts had a lower onset potential (enhanced activity) for oxygen evolution than the homo Co_2/N_4G catalyst ($U_{onset} = 1.69$ V). Especially, the CoCu/N_4G catalyst exhibited a significant improvement in OER activity compared to the other hetero double-atom cases. This enhancement was related to the large reduction in the affinity of the reaction intermediates (O*, OH*, and OOH*) [ΔE_{ads}(O*) = −4.27 eV, ΔE_{ads}(OH*) = −3.47 eV, and ΔE_{ads}(OOH*) = −2.06

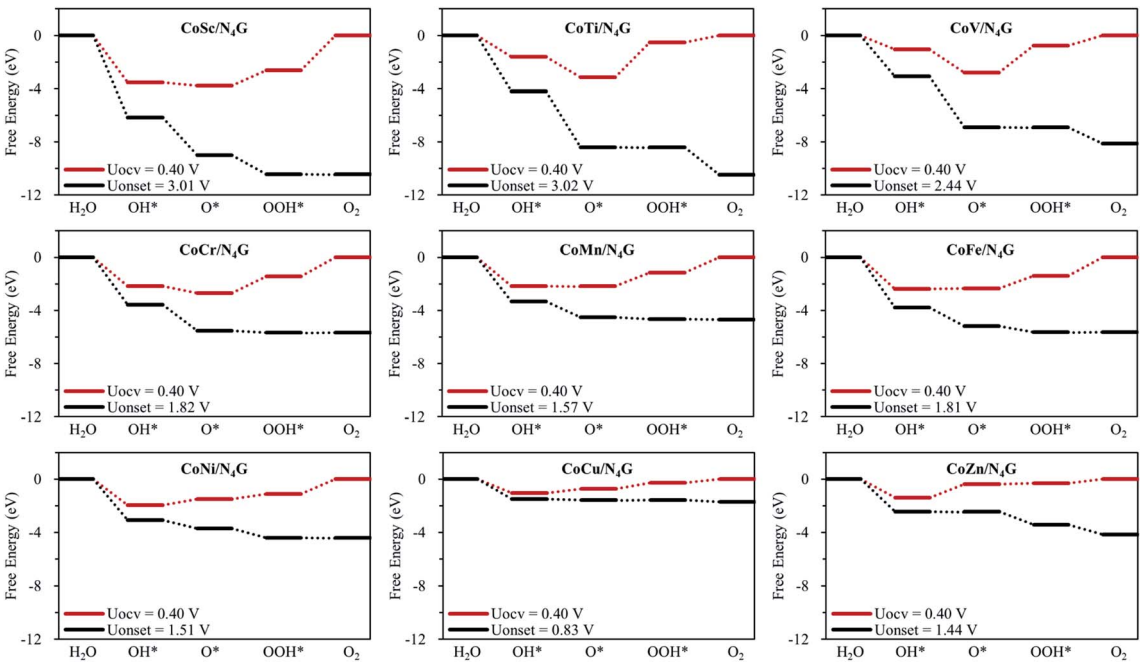

Fig. 3 Free energy diagrams for CoM/N_4G (M = 3d block metals) at OCV condition ($U_{OCV} = 0.401$ V) and onset potential.

Table 2 Adsorption energies (ΔE_{ads}) of the intermediates in units of [eV], and the onset potential (U_{onset}) for the CoM/N_4G catalysts

Catalyst	ΔE_{ads}(O*)	ΔE_{ads}(OH*)	ΔE_{ads}(OOH*)	U_{onset} (V)
CoSc/N_4G	−7.33	−5.95	−4.38	3.01
CoTi/N_4G	−6.71	−4.01	−2.30	3.02
CoV/N_4G	−6.37	−3.44	−2.55	2.44
CoCr/N_4G	−6.26	−4.57	−3.19	1.82
CoMn/N_4G	−5.74	−4.56	−2.94	1.57
CoFe/N_4G	−5.90	−4.79	−3.18	1.81
Co_2/N_4G	−5.86	−4.48	−3.06	1.69
CoNi/N_4G	−5.04	−4.37	−2.87	1.51
CoCu/N_4G	−4.27	−3.47	−2.06	0.83
CoZn/N_4G	−3.92	−3.82	−2.06	1.44

eV] (see Table 2) on the CoCu/N_4G catalyst than for the homo Co_2 double-atom case [ΔE_{ads}(O*) = −5.86 eV, ΔE_{ads}(OH*) = −4.48 eV, and ΔE_{ads}(OOH*) = −3.06 eV], which resulted in a shift of the PLS from OOH* + OH^- → * + $O_{2(g)}$ + $H_2O_{(l)}$ + e^- to O* + OH^- → OOH* + e^- and a decrease in the endothermicity of the PLS.

On the other hand, for the CoSc (U_{onset} = 3.01 V), CoTi (U_{onset} = 3.02 V), CoV (U_{onset} = 2.44 V), and CoFe (U_{onset} = 1.81 V) cases, the onset potential increased (OER activity decreased) due to the substantial increase in the affinity of the reaction intermediates (particularly, O*). Note the adsorption energies for CoSc [ΔE_{ads}(O*) = −7.33 eV, ΔE_{ads}(OH*) = −5.95 eV, and ΔE_{ads}(OOH*) = −4.38 eV], CoTi [ΔE_{ads}(O*) = −6.71 eV, ΔE_{ads}(OH*) = −4.01 eV, and ΔE_{ads}(OOH*) = −2.30 eV], CoV [ΔE_{ads}(O*) = −6.37 eV, ΔE_{ads}(OH*) = −3.44 eV, and ΔE_{ads}(OOH*) = −2.55 eV], and CoFe [ΔE_{ads}(O*) = −5.90 eV, ΔE_{ads}(OH*) = −4.79 eV, and ΔE_{ads}(OOH*) = −3.18 eV] (see Table 2). The most favorable adsorption configurations of CoM/N_4G are shown in Fig. S3.†

Fig. 4 and S4† display the variation of the onset potential as a function of O*, OH*, OOH* adsorption energy for the homo Co_2/N_4G and hetero CoM/N_4G catalysts. We discovered that a key descriptor representing the electrocatalytic activity for the OER was the O* binding energy [note the clear volcanic correlation between U_{onset} and ΔE_{ads}(O*)]. Here, the volcano plot [U_{onset} *versus* ΔE_{ads}(O*)] demonstrated that the OER activity could be increased when the ΔE_{ads}(O*) = −5.86 eV of a homo Co_2/N_4G catalyst rose to the peak position of about −4.37 eV, whereas the activity decreased when the ΔE_{ads}(O*) further decreased over the peak position. Therefore, indicating that there was still a probability to develop new CoM/N_4G catalysts surpassing the OER performance of the CoCu/N_4G catalyst.

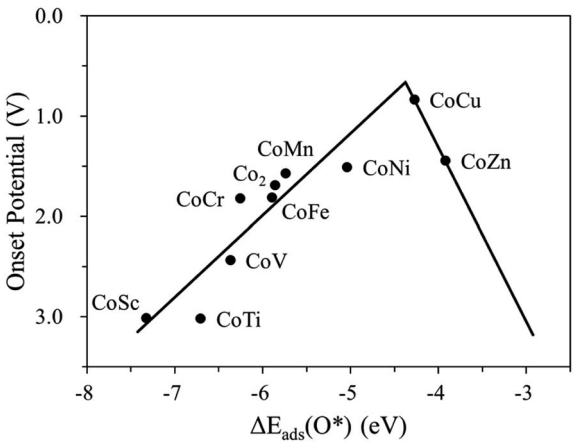

Fig. 4 Volcano curve indicating the activity (onset potential) for the CoM/N_4G catalysts (M = 3d block metals) depending on the oxygen adsorption energy, ΔE_{ads}(O*).

In addition to the N_4G support material, we investigated the OER activity when the N_4G support (which had a di-vacancy of two carbon atoms surrounded by four nitrogen atoms) (Fig. S5†) was replaced by the N_5G support (which had two mono-vacancies, and five nitrogen atoms covering the edge site of two mono-vacancies) (Fig. S5†) to examine the support vacancy arrangement effect on the activity of hetero CoCu double-atom catalyst. We found out that the most active CoCu double atoms in the N_5G support stably existed when Co and Cu atoms were in each mono-vacancy site, and Co and Cu atoms were bound horizontally to each other (Fig. S5†). The result of the OER activity prediction showed that the hetero CoCu/N_5G catalyst had a higher onset potential (U_{onset} = 1.25 V) than CoCu/N_4G (U_{onset} = 0.83 V). The decreased OER activity of CoCu/N_5G came from the increase in O* binding strength as well as the reduction of the OOH* affinity. Note the adsorption energies for CoCu/N_5G [ΔE_{ads}(O*) = −4.45 eV, ΔE_{ads}(OH*) = −3.14 eV, and ΔE_{ads}(OOH*) = −1.81 eV]. Thus, the endothermicity of the free energy change at the PLS (O* + OH^- → OOH* + e^-) increased (see Fig. S6†) and in turn the OER activity was reduced. In addition, our DFT calculations showed the higher stability (formation energy) of di-vacancy by 6.12 eV than for the two mono-vacancy systems. Note that we considered the N_4G + N → N_5G + C reaction for calculation of the formation energy difference.

Origin of the enhanced OER activity in the hetero double-atoms catalysts

To better understand the role of the Cu atom in the hetero CoCu/N_4G catalyst in boosting OER activity, we attempted to decouple the strain, dopant, and configurational effects in a CoCu/N_4G catalyst. Note that the OER activity of the hetero CoCu/N_4G catalyst compared to the homo Co_2/N_4G case could be changed by the three effects.[58–60] The first factor (the so-called strain effect) was related to the atomic size mismatch between the Co and Cu atom in the hetero CoCu/N_4G catalyst, which could affect the d-band structure and in turn the surface reactivity. The second one (the so-called dopant effect) was related to the modification in the d-band states of both Cu and Co atoms induced by the mixing of valence electrons between Cu and Co atoms.[61,62] The last one (the so-called configurational effect) was related to the modification of the catalytic activity caused by the ensemble structure change of the CoCu dimer by the strong interaction between the hetero CoCu double atom and the nitrogen-doped graphene. As shown in Fig. 5(a), when the homo Co_2/N_4G catalyst turned into the hetero CoCu/N_4G system, the Co_2/N_4G catalyst underwent the above three effects in series. The first change of the inclined hexagon Co double

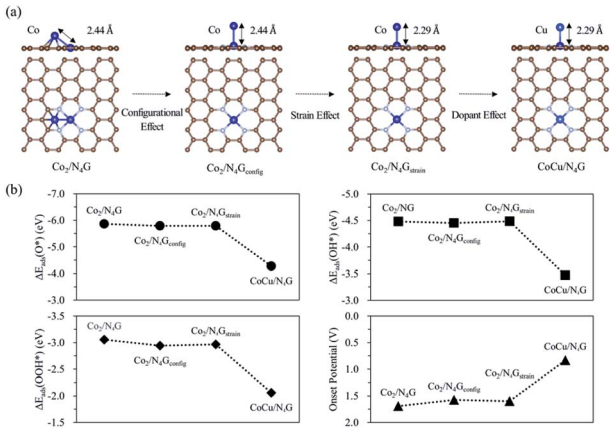

Fig. 5 (a) Decoupled models of the configurational (Co_2/N_4G_{config}), strain (Co_2/N_4G_{strain}) and dopant effects. (b) Adsorption energy and onset potential variation of each decoupled model.

atom (Co_2/N_4G) into the vertical Co double atom (as indicated by the Co_2/N_4G_{config} model) represented the contribution of the configurational effect to the total OER activity. Here, the bond distance between Co atoms in the Co_2/N_4G_{config} model (2.44 Å) was the same as the Co_2/N_4G case. Our DFT calculations predicted that the affinity of the reaction intermediates on the Co_2/N_4G_{config} model was slightly decreased by 0.03∼0.12 eV compared to the Co_2/N_4G case. Note $\Delta E_{ads}(O^*) = -5.86$ eV, $\Delta E_{ads}(OH^*) = -4.48$ eV, $\Delta E_{ads}(OOH^*) = -3.06$ eV for the Co_2/N_4G catalyst, while $\Delta E_{ads}(O^*) = -5.79$ eV, $\Delta E_{ads}(OH^*) = -4.45$ eV, $\Delta E_{ads}(OOH^*) = -2.94$ eV for the Co_2/N_4G_{config} catalyst [See Fig. 5(b)]. As a result, the onset potential of the Co_2/N_4G_{config} model was slightly decreased by 0.11 V, suggesting that the configurational effect tended to raise the OER activity.

The second change of the Co_2/N_4G_{config} model to the compressively strained vertical Co double atom (referred to the Co_2/N_4G_{strain} model) indicated the relative contribution of the strain effect to the total OER catalysis. Here, the Co–Co bond of the Co_2/N_4G_{strain} model was 2.29 Å (whose bond length was the same as the Co–Cu bond of the stable $CoCu/N_4G$ catalyst), which was contracted by 6.15% compared to the Co_2/N_4G_{config} model. We saw almost no change of the binding strength for all reaction intermediates [$\Delta E_{ads}(O^*) = -5.79$ eV, $\Delta E_{ads}(OH^*) = -4.48$ eV, $\Delta E_{ads}(OOH^*) = -2.97$ eV] for the Co_2/N_4G_{strain} model compared to the Co_2/N_4G_{config} case. Here, although there was a relatively large compressive strain effect on the Co_2 double atom, the adsorption energies were little changed. This may come from the adsorption states of the intermediates where only the top Co atom in the vertical Co double atom actively interacted with the intermediates, such that the strain effect may hardly affect the affinity for the intermediates (see Fig. S7†). Accordingly, the OER activity of the Co_2/N_4G_{strain} model (the onset potential = 1.60 V) was almost the same as for the Co_2/N_4G_{config} model (the onset potential = 1.58 V), implying that the strain effect was not important in determining the OER catalysis. Finally, a top Co atom of Co_2/N_4G_{strain} model was substituted for a Cu atom as it maintained the bond distance of 2.29 Å ($CoCu/N_4G$ model), which could help understanding the Cu dopant effect on the total OER activity. Our DFT calculations showed the great reduction in the affinity of the reaction intermediates by the dopant effect. For example, the $\Delta E_{ads}(O^*)$ of $CoCu/N_4G$ was reduced by 1.52 eV in comparison with the Co_2/N_4G_{strain} model. Similarly, the $CoCu/N_4G$ catalyst had strikingly higher OH* (−3.47 eV) and OOH* (−2.06 eV) adsorption energies than the Co_2/N_4G_{strain} case [$\Delta E_{ads}(OH^*) = -4.48$ eV, and $\Delta E_{ads}(OOH^*) = -2.97$ eV]. This large reduction of adsorption strength gave rise to a considerable decrease in the free energy change of the potential limiting step. Thus, the OER activity was significantly enhanced with the onset potential of 0.83 V. These results demonstrated that the dopant effect was critical for boosting the OER activity, while the configurational and strain effects played a minor role.

Next, to precisely comprehend the fundamental properties relevant to the OER catalysis, we predicted the d-orbital resolved density of states (ORDOS) (d_{z^2}, d_{xz}, d_{yz}, d_{xy}, and $d_{x^2-y^2}$) of the Co and Cu atoms and the p density of states (DOS) of the O atom for the O-adsorbed homo Co_2/N_4G and hetero $CoCu/N_4G$ catalysts (see Fig. 6). For validity of this analysis, the precedent work about the hetero double-atom catalysts for electrochemical NH_3 production has been already reported and its validity proven.[37] Here, the oxygen adsorption structure is key to the understanding of the descriptor for representing the OER activity as mentioned in previous section. For the homo Co_2/N_4G catalyst, we identified a strong overlap between the d_{z^2}, d_{xz}, d_{yz}, d_{xy}, and $d_{x^2-y^2}$ orbitals of the Co dimers and the p orbital of the O atom in the energy ranges from −4.80 to −3.60, from −3.40 to −2.90, from −2.50 to −2.05, and from −1.10 eV to −0.50 eV. To understand the degree of orbital overlap quantitatively, the overlap ratio (X_d), which denotes the fraction of p–d orbital overlap in the total p orbital, was estimated as shown in Fig. 7. We found that the d_{z^2}, d_{xz}, and d_{yz} orbitals, which feature an orientation toward z-direction, were closely involved in the bonding to the oxygen compared to the $d_{x^2-y^2}$ and d_{xy} for the homo Co_2/N_4G catalyst. Note that the order of overlap was d_{xz} ($X_d = 0.37$) > d_{z^2} ($X_d = 0.35$) > d_{yz} ($X_d = 0.32$) ≫ $d_{x^2-y^2}$ ($X_d = 0.12$) > d_{xy} ($X_d = 0.11$). On the other hand, for the hetero $CoCu/N_4G$ case, the pattern of orbital overlap was greatly different from the

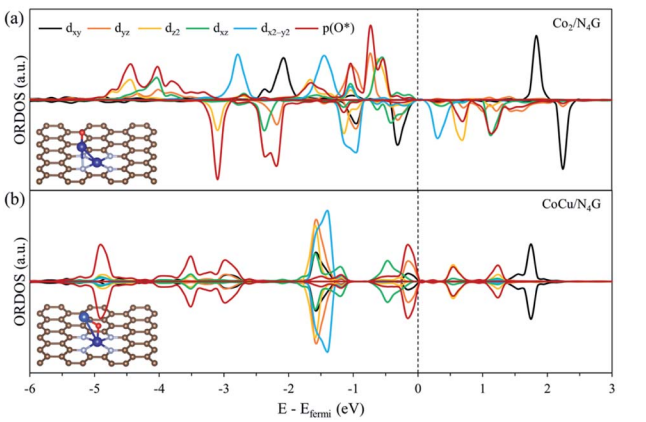

Fig. 6 The d-orbital resolved density of state (ORDOS) analysis of the oxygen adsorbed (a) Co_2/N_4G and (b) $CoCu/N_4G$.

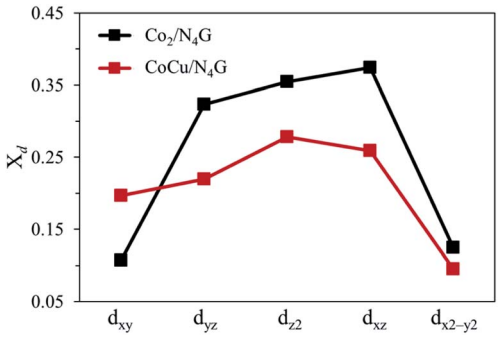

Fig. 7 Overlap ratio (X_d) of d-orbitals to p-orbitals. The black dots correspond to the overlap ratio of Co_2/N_4G, and the red dots are equivalent to the overlap ratio of CoCu/N_4G.

homo Co_2/N_4G catalyst. Note the overlap energy ranged from −5.10 to −4.80, from −3.70 to −2.75, from −1.60 to −1.10, and from −0.25 eV to −0.0 eV for the hetero CoCu/N_4G catalyst in Fig. 6(b). This led to a change in the key orbitals in determining the oxygen adsorption process. That is, in addition to the d_{z^2} (X_d = 0.28), d_{xz} (X_d = 0.26), and d_{yz} (X_d = 0.22) orbitals, the d_{xy} (X_d = 0.20) orbital was actively involved in oxygen adsorption. Here, the activation of d_{xy} in the hetero CoCu/N_4G catalyst was associated with the adsorption of an oxygen atom at the bridge site of the vertical CoCu double atom. Note that the p orbital of oxygen could strongly interact with the d_{xy} (X_d = 0.20) orbital of the Cu atom, as shown in Fig. 7. In addition to the activation of the d_{xy} orbital, another noticeable change was observed in the CoCu/N_4G catalyst. Even though an additional orbital of d_{xy} was involved in the adsorption process, the overlap ratio of most of the key orbitals (d_{z^2}, d_{xz} and d_{yz}) decreased, which means the interaction between CoCu atoms and O atom was reduced in comparison with Co_2. As a result, the decrease in the overlap ratio of d_{z^2}, d_{xz} and d_{yz} orbitals made the oxygen adsorption weak (see Table 2).

Computational screening for the hetero CoM (M = 4d, 5d block metals) double-atoms

Next, to find another hetero double-atom catalyst, we searched the possible dopants that could enhance the OER activity of the hetero CoM (M = 4d and 5d block metals) double-atom catalysts supported on the defective N-doped graphene. For such a purpose, as discussed in the 3d dopant case, we first

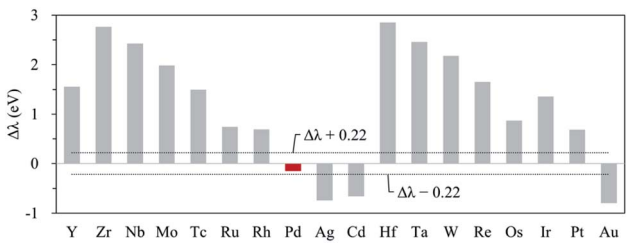

Fig. 8 Relative descriptor value (Δλ) of CoM/N_4G (M = 4d, 5d block metals). The black dotted line denotes the range for selecting candidates (−0.22 eV < Δλ < 0.22 eV), and left column means the candidate M chosen within the range.

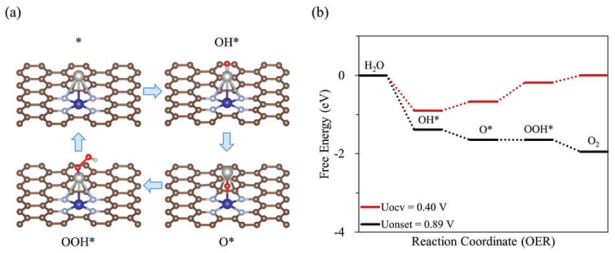

Fig. 9 (a) Schematic diagram of OER on the CoPd/N_4G catalyst with the most favorable adsorption configuration of each intermediate, (b) the free energy diagram for the OER on the CoPd/N_4G catalyst at OCV and the onset potential.

determined the thermodynamically stable structure of the hetero CoM (M = 4d and 5d block metals)/N_4G catalyst (based on the formation energy) and then calculated the descriptor [which is ΔE_{ads}(O*) and denoted as λ] on the surface of the stable CoM/N_4G catalysts. Fig. 8 depicts the relative descriptor value (indicated by Δλ), which is defined as the deviation from the peak position ($\lambda = -4.37$ eV) in the volcano plot of Fig. 4. We saw a large variation of Δλ as the dopant type changes. Here, we selected a promising CoPd/N_4G candidate whose λ was placed near the peak position (−0.22 eV < Δλ < 0.22 eV). Fig. 9 shows the molecular configuration of the reaction intermediates and the free energy diagram for the OER on the proposed CoPd/N_4G catalyst. Our DFT calculations predicted a reduced onset potential by 0.80 V (U_{onset} = 0.89 V) compared to the homo Co_2/N_4G catalyst, suggesting the improved OER activity.

Conclusions

Using spin-polarized density functional theory (DFT) calculations, we investigated the electrochemical water oxidation on Co-based homo and hetero double-atom catalysts under alkaline conditions. The following is the summary findings from our study.

(1) The ensemble structures of the Co-based homo and double atom catalysts supported on nitrogen-doped graphene (CoM/N_4G) were examined based on their nine possible configurations (C1–C9) and determined by the formation energy. We confirmed that the most stable structures of the CoM/N_4G catalysts converged into three geometries: C1 (vertical Co double-atom shape) (CoCr, CoMn, CoFe, CoCu, CoZn); C2 (vertical M double-atom shape) (CoTi, CoV); and C4 (inclined hexagon M double-atom shape) (CoSc, CoNi).

(2) The OER activity of CoM/N_4G (M = 3d block metals) was predicted based on the reaction mechanism under alkaline conditions. We discovered hetero CoCu, CoMn, CoNi, and CoZn double-atom catalysts had advanced activity compared to the homo Co_2 double-atom catalyst. In particular, the hetero CoCu/N_4G double-atom catalyst showed a strikingly lower onset potential by 0.86 V (U_{onset} = 0.83 V) than the Co_2/N_4G (U_{onset} = 1.69 V) case, which was related to the PLS shift from the OOH* → $O_{2(g)}$ step [Co_2/N_4G] to the O* → OOH* step and in turn the decrease in the endothermicity in PLS owing to the large reduction in the affinity of the reaction intermediates.

(3) The origin of the boosted activity of the hetero $CoCu/N_4G$ double-atom catalyst was described by the decoupled strain (bond length change of the double atom), dopant (substitute Co atom for Cu atom), and configurational (ensemble structure alteration) effects. Decoupling of the effects revealed that the dopant Cu atom, where the d-band states of both the Cu and Co atoms were modified by valence electrons mixing, had a great impact on improving the OER performance by decreasing the adsorption strength of O*, OH*, and OOH*, whereas the strain and configurational effect had only a slight influence on the activity or barely affected the variation of the onset potential. The weakened adsorption strength was also explained by the d-orbital resolved density of states (ORDOS) (d_{z^2}, d_{xz}, d_{yz}, d_{xy}, and $d_{x^2-y^2}$) of the double-metal atom and p density of states (DOS) of the adsorbed O atom, and the degree of overlap was quantitatively estimated by the p–d orbital overlap ratio (X_d). We found that the overlap ratio of the key orbitals for the homo Co_2/N_4G catalyst, which was characterized by the *z*-direction involved orbitals (d_{z^2}, d_{xz}, and d_{yz}), exhibited a higher overlap ratio [d_{z^2} ($X_d = 0.35$), d_{xz} ($X_d = 0.37$) and d_{yz} ($X_d = 0.32$)] than the $CoCu/N_4G$ case. On the other hand, a distinctive change in the overlap ratio for the hetero $CoCu/N_4G$ catalyst, where the key orbitals were the d_{z^2} ($X_d = 0.28$), d_{xz} ($X_d = 0.26$), d_{yz} ($X_d = 0.22$), and d_{xy} ($X_d = 0.20$), was verified. As a result, a drop in the binding strength of the O atom arose in the hetero $CoCu/N_4G$ catalyst.

(4) Finally, we explored other dopants to improve the OER activity of the hetero CoM (M = 4d and 5d block metals) double-atom catalysts using the descriptor [ΔE_{ads}(O*) or λ] determined by volcano curve. The promising $CoPd/N_4G$ candidate was chosen by the deviation ($\Delta\lambda$) range from −0.22 eV to 0.22 eV on the basis of the peak position ($\lambda = -4.37$ eV). The onset potential of the selected $CoPd/N_4G$ catalyst presented a reduced onset potential by 0.80 V as compared to the homo Co_2/N_4G catalyst, verifying the suitability of the descriptor. It implied that there is still a chance to discover another efficient hetero double-atom catalyst having the descriptor value near the peak position.

In conclusion, our theoretical study offers useful insights into developing a strategy for high-efficiency OER catalysts using a variety of double-atom composites for the future.

Conflicts of interest

There are no conflicts to declare.

Acknowledgements

This work was financially supported by the National Research Foundation of Korea (NRF) grant funded by the Korea government (MSIT) (No. NRF-2021M3I3A1084813, NRF-2020R1A2C1099711). This work was also financially supported by Korea Institute of Science and Technology (KIST) and Inha University Research Grant.

References

1 J. Chi and H. Yu, *Chin. J. Catal.*, 2018, **39**, 390–394.
2 J. Brauns and T. Turek, *Processes*, 2020, **8**, 248.
3 F. Barbir, *Sol. Energy*, 2005, **78**, 661–669.
4 S. S. Kumar and V. Himabindu, *Mater. Sci. Energy Technol.*, 2019, **2**, 442–454.
5 L. Zhuang, L. Ge, Y. Yang, M. Li, Y. Jia, X. Yao and Z. Zhu, *Adv. Mater.*, 2017, **29**, 1606793.
6 K. Zhu, T. Wu, M. Li, R. Lu, X. Zhu and W. Yang, *J. Mater. Chem. A*, 2017, **5**, 19836–19845.
7 H. Xu, H. Shang, C. Wang, L. Jin, C. Chen, C. Wang and Y. Du, *Appl. Catal., B*, 2020, **265**, 118605.
8 Y. Liu, H. Cheng, M. Lyu, S. Fan, Q. Liu, W. Zhang, Y. Zhi, C. Wang, C. Xiao and S. Wei, *J. Am. Chem. Soc.*, 2014, **136**, 15670–15675.
9 T. Reier, M. Oezaslan and P. Strasser, *ACS Catal.*, 2012, **2**, 1765–1772.
10 Y. Lee, J. Suntivich, K. J. May, E. E. Perry and Y. Shao-Horn, *J. Phys. Chem. Lett.*, 2012, **3**, 399–404.
11 T. Reier, Z. Pawolek, S. Cherevko, M. Bruns, T. Jones, D. Teschner, S. r. Selve, A. Bergmann, H. N. Nong and R. Schlögl, *J. Am. Chem. Soc.*, 2015, **137**, 13031–13040.
12 L. Zhang, Q. Fan, K. Li, S. Zhang and X. Ma, *Sustainable Energy Fuels*, 2020, **4**, 5417–5432.
13 J. Luo, L. Wang, D. Mott, P. N. Njoki, N. Kariuki, C.-J. Zhong and T. He, *J. Mater. Chem.*, 2006, **16**, 1665–1673.
14 K. Bergamaski, A. L. Pinheiro, E. Teixeira-Neto and F. C. Nart, *J. Phys. Chem. B*, 2006, **110**, 19271–19279.
15 R. A. Hameed and S. S. Medany, *J. Colloid Interface Sci.*, 2018, **513**, 536–548.
16 J. N. Stuecker, J. E. Miller, R. E. Ferrizz, J. E. Mudd and J. Cesarano, *Ind. Eng. Chem. Res.*, 2004, **43**, 51–55.
17 R. H. Tammam, A. M. Fekry and M. M. Saleh, *Korean J. Chem. Eng.*, 2019, **36**, 1932–1939.
18 H. Sim, J. Lee, T. Yu and B. Lim, *Korean J. Chem. Eng.*, 2018, **35**, 257–262.
19 K. Min, S. Kim, E. Lee, G. Yoo, H. C. Ham, S. E. Shim, D. Lim and S.-H. Baeck, *J. Mater. Chem. A*, 2021, **9**, 17344–17352.
20 K. Min, M. Hwang, S. E. Shim, D. Lim and S.-H. Baeck, *Chem. Eng. J.*, 2021, **424**, 130400.
21 H. J. Qiu, Y. Ito, W. Cong, Y. Tan, P. Liu, A. Hirata, T. Fujita, Z. Tang and M. Chen, *Angew. Chem., Int. Ed.*, 2015, **54**, 14031–14035.
22 Y. Chen, S. Ji, C. Chen, Q. Peng, D. Wang and Y. Li, *Joule*, 2018, **2**, 1242–1264.
23 C. Zhu, Q. Shi, S. Feng, D. Du and Y. Lin, *ACS Energy Lett.*, 2018, **3**, 1713–1721.
24 X.-F. Yang, A. Wang, B. Qiao, J. Li, J. Liu and T. Zhang, *Acc. Chem. Res.*, 2013, **46**, 1740–1748.
25 Y. Peng, B. Lu and S. Chen, *Adv. Mater.*, 2018, **30**, 1801995.
26 N. Cheng, L. Zhang, K. Doyle-Davis and X. Sun, *Electrochem. Energy Rev.*, 2019, **2**, 539–573.
27 H. Zhang, G. Liu, L. Shi and J. Ye, *Adv. Energy Mater.*, 2018, **8**, 1701343.
28 A. Wang, J. Li and T. Zhang, *Nat. Rev. Chem.*, 2018, **2**, 65–81.
29 A. Morozan, V. Goellner, Y. Nedellec, J. Hannauer and F. Jaouen, *J. Electrochem. Soc.*, 2015, **162**, H719.
30 M. D. Hossain, Z. Liu, M. Zhuang, X. Yan, G. L. Xu, C. A. Gadre, A. Tyagi, I. H. Abidi, C. J. Sun and H. Wong, *Adv. Energy Mater.*, 2019, **9**, 1803689.

31 L. Osmieri, R. Escudero-Cid, A. H. M. Videla, P. Ocón and S. Specchia, *Appl. Catal., B*, 2017, **201**, 253–265.
32 M. M. Hossen, K. Artyushkova, P. Atanassov and A. Serov, *J. Power Sources*, 2018, **375**, 214–221.
33 S. Dilpazir, H. He, Z. Li, M. Wang, P. Lu, R. Liu, Z. Xie, D. Gao and G. Zhang, *ACS Appl. Energy Mater.*, 2018, **1**, 3283–3291.
34 Z. Geng, Y. Liu, X. Kong, P. Li, K. Li, Z. Liu, J. Du, M. Shu, R. Si and J. Zeng, *Adv. Mater.*, 2018, **30**, 1803498.
35 J. Wang, Z. Huang, W. Liu, C. Chang, H. Tang, Z. Li, W. Chen, C. Jia, T. Yao and S. Wei, *J. Am. Chem. Soc.*, 2017, **139**, 17281–17284.
36 Y. Li, H. Su, S. H. Chan and Q. Sun, *ACS Catal.*, 2015, **5**, 6658–6664.
37 S.-h. Kim, H. C. Song, S. J. Yoo, J. Han, K.-Y. Lee and H. C. Ham, *J. Mater. Chem. A*, 2022, **10**, 6216–6230.
38 X.-Q. Han, Z.-L. Lang, F.-Y. Zhang, H.-L. Xu and Z.-M. Su, *Appl. Surf. Sci.*, 2022, **579**, 152214.
39 X. Lv, W. Wei, B. Huang, Y. Dai and T. Frauenheim, *Nano Lett.*, 2021, **21**, 1871–1878.
40 H. Li, Z. Zhao, Q. Cai, L. Yin and J. Zhao, *J. Mater. Chem. A*, 2020, **8**, 4533–4543.
41 W. Yang, H. Huang, X. Ding, Z. Ding, C. Wu, I. D. Gates and Z. Gao, *Electrochim. Acta*, 2020, **335**, 135667.
42 H. Yan, Y. Lin, H. Wu, W. Zhang, Z. Sun, H. Cheng, W. Liu, C. Wang, J. Li and X. Huang, *Nat. Commun.*, 2017, **8**, 1–11.
43 P.-F. Yuan, H. Liu, Q. Sun and Y. Jia, *Comput. Mater. Sci.*, 2018, **151**, 189–195.
44 Q. Luo, W. Zhang, C.-F. Fu and J. Yang, *Int. J. Hydrogen Energy*, 2018, **43**, 6997–7006.
45 G. Kresse and J. Furthmüller, *Phys. Rev. B: Condens. Matter Mater. Phys.*, 1996, **54**, 11169.
46 J. P. Perdew, J. A. Chevary, S. H. Vosko, K. A. Jackson, M. R. Pederson, D. J. Singh and C. Fiolhais, *Phys. Rev. B: Condens. Matter Mater. Phys.*, 1992, **46**, 6671.
47 J. P. Perdew and A. Zunger, *Phys. Rev. B: Condens. Matter Mater. Phys.*, 1981, **23**, 5048.
48 J. P. Perdew, K. Burke and M. Ernzerhof, *Phys. Rev. Lett.*, 1996, **77**, 3865.
49 P. E. Blöchl, *Phys. Rev. B: Condens. Matter Mater. Phys.*, 1994, **50**, 17953.
50 H. J. Monkhorst and J. D. Pack, *Phys. Rev. B: Solid State*, 1976, **13**, 5188.
51 H. Niu, X. Wang, C. Shao, Z. Zhang and Y. Guo, *ACS Sustainable Chem. Eng.*, 2020, **8**, 13749–13758.
52 X. Zhai, L. Li, X. Liu, Y. Li, J. Yang, D. Yang, J. Zhang, H. Yan and G. Ge, *Nanoscale*, 2020, **12**, 10035–10043.
53 Z. Xu, R. Song, M. Wang, X. Zhang, G. Liu and G. Qiao, *Phys. Chem. Chem. Phys.*, 2020, **22**, 26223–26230.
54 J. K. Nørskov, J. Rossmeisl, A. Logadottir, L. Lindqvist, J. R. Kitchin, T. Bligaard and H. Jonsson, *J. Phys. Chem. B*, 2004, **108**, 17886–17892.
55 Q. Liang, G. Brocks and A. Bieberle-Hütter, *J. Phys.: Energy*, 2021, **3**, 026001.
56 M. Plevová, J. Hnát and K. Bouzek, *J. Power Sources*, 2021, 230072.
57 C. Hu, L. Zhang and J. Gong, *Energy Environ. Sci.*, 2019, **12**, 2620–2645.
58 M. Mavrikakis, B. Hammer and J. K. Nørskov, *Phys. Rev. Lett.*, 1998, **81**, 2819.
59 P. Strasser, S. Koh, T. Anniyev, J. Greeley, K. More, C. Yu, Z. Liu, S. Kaya, D. Nordlund and H. Ogasawara, *Nat. Chem.*, 2010, **2**, 454–460.
60 A. Khorshidi, J. Violet, J. Hashemi and A. A. Peterson, *Nat. Catal.*, 2018, **1**, 263–268.
61 T. Bligaard and J. K. Nørskov, *Electrochim. Acta*, 2007, **52**, 5512–5516.
62 H. Kim, H. Park, H. Bang and S.-K. Kim, *Korean J. Chem. Eng.*, 2020, **37**, 1275–1294.